J. Iron Steel Res. Int. (2019) 26:761–770
https://doi.org/10.1007/s42243-019-00274-2

ORIGINAL PAPER

Correlation between microstructure and impact toughness of weld heat-affected zone in 5 wt.% manganese steels

Jun-hui Li[1] · Hong-hong Wang[1] · Qiang Luo[1] · Li Li[2] · Chao Sun[2] · R.D.K. Misra[3]

Received: 2 March 2018 / Revised: 6 October 2018 / Accepted: 10 October 2018 / Published online: 21 May 2019

Abstract
The microstructure in welding heat-affected zones of 5 wt.% manganese steels was studied, and its effect on impact toughness was analyzed. The simulated coarse-grained heat-affected zone (CGHAZ) had the lowest impact toughness of ~ 39 J at − 40 °C because of coarse-grained structure and least volume fraction of retained austenite (RA) of 1.2 vol.%. The impact toughness of simulated intercritical heat-affected zone (ICHAZ) and fine-grained heat-affected zone (FGHAZ) were ~ 165 and ~ 45 J, respectively, at − 40 °C. The effective grain size of simulated FGHAZ was smaller than that of the simulated ICHAZ. Furthermore, microstructural investigation revealed that the simulated FGHAZ and ICHAZ had similarity in volume fraction and stability of RA. However, tempered martensite was present in ICHAZ and absent in FGHAZ. It is proposed that the presence of tempered martensite contributed to good impact toughness in simulated ICHAZ.

Keywords 5 wt.% manganese steel · Welding heat-affected zone · Retained austenite · Tempered martensite · Impact toughness

1 Introduction

Medium manganese steels (3–12 wt.% Mn) are receiving significant attention as third-generation advanced high-strength steels [1, 2]. It is suggested that medium-Mn steels are potential candidates that meet the mechanical properties by varying Mn content and intercritical annealing involving austenite reverted transformation [3]. Mn is an important alloying element in the design of advanced high-strength steels, because it increases the stability of austenite and also impacts the kinetics of transformation [4, 5]. Super low-carbon medium-Mn steels have been developed for the use in ship hull, bridges, buildings, pressure vessels, and off-shore structures [6] because of their excellent combination of high strength and impact toughness at relatively low temperature. Mn can significantly improve hardenability and thereby enhance the homogeneity along the thickness in terms of microstructure and properties of the mid-thick steel plate [7, 8]. The desired microstructure is expected to be dual-phase structure of metastable austenite (retained austenite, RA) and martensite. Fine martensitic plates containing high dislocation density contribute to strength. High strain hardenability of RA provides ductility and toughness [9–11]. It was demonstrated that the morphology and volume fraction of metastable austenite are governed by heat treatment parameters, such as temperature, holding time and cooling rate [12, 13].

In application of super low-carbon medium-Mn steel, arc welding is a dominant joining technology for mid-thickness plates. Welding thermal cycle is inevitable and results in dramatic changes in the microstructure and final mechanical properties, especially low-temperature impact toughness in heat-affected zone (HAZ). Different welding thermal cycles have different peak temperatures and

✉ Hong-hong Wang
wanghonghong@wust.edu.cn

[1] The State Key Laboratory of Refractories and Metallurgy, Wuhan University of Science and Technology, Wuhan 430081, Hubei, China

[2] Research Institute of Nanjing Iron and Steel Co., Ltd., Nanjing 210035, Jiangsu, China

[3] Laboratory for Excellence in Advanced Steel Research, Department of Metallurgical, Materials and Biomedical Engineering, University of Texas at El Paso, El Paso, TX 79968, USA

cooling rates. Increased cooling rate will lower A_{r1} and A_{r3} temperatures [14, 15], which will lead to changes in the composition of the microstructure [16, 17] and result in stability of retained austenite [18–21]. Yoo et al. [22] studied the correlation between microstructure and mechanical properties of heat-affected zones in Fe–8Mn–0.06C steel. They indicated that the existence of retained austenite provided the beneficial effect on the impact toughness. Coarse-grained heat-affected zone (CGHAZ) was "localized embrittlement zone" due to the undetectable austenite content and coarsening of the crystal grains. Fine-grained heat-affected zone (FGHAZ) and intercritical heat-affected zone (ICHAZ) were determined by the different retained austenite content. However, the evolution of microstructure, and especially retained austenite by welding thermal cycles in medium-Mn steels remained unclear. Therefore, it is necessary to investigate microstructural evolution during welding thermal cycle to correlate microstructure and impact toughness.

In the present study, the microstructural evolution including RA and martensite by welding thermal cycle is investigated in advanced low-carbon 5 wt.% manganese steel. The change in impact toughness is elucidated based on phase transformation and microstructural evolution.

2 Experimental procedure

The experimental material was an advanced 5Mn steel. The chemical composition and mechanical properties are shown in Tables 1 and 2. After quenching and intercritical tempering, the microstructure consisted of tempered martensite and 16.5 wt.% RA. DIL805A dilatometer was performed to measure the linear expansion-temperature curve on heating. Start transformation temperature A_{c1} and finish temperature A_{c3} on heating were measured to be (626 ± 5) °C and (790 ± 5) °C. The lever law was used to estimate the volume fraction of austenite phase on heating.

Gleeble 3800 was used to simulate welding thermal cycle and to produce weld HAZs. Specimens of dimensions 11 mm × 11 mm × 70 mm were prepared. Based on A_{c1} and A_{c3} temperature obtained from dilatometry tests, 1320 °C was set to simulate CGHAZ, 840 °C for FGHAZ and 710 °C for ICHAZ. The specific thermal simulation processes are shown in Fig. 1.

Following the thermal cycling treatment, specimen blanks were machined to final dimensions of 10 mm × 10 mm × 55 mm and notched. Impact energy at − 40 °C was measured using a Charpy V-notch impact testing machine.

Table 2 Mechanical properties of 5Mn steel

R_{eL}/MPa	R_m/MPa	A/%	Yield ratio	KV_2 (− 60 °C)/J
649	773	26	0.85	203

R_{eL} Yield strength; R_m tensile strength; A elongation; KV_2 absorbed impact energy

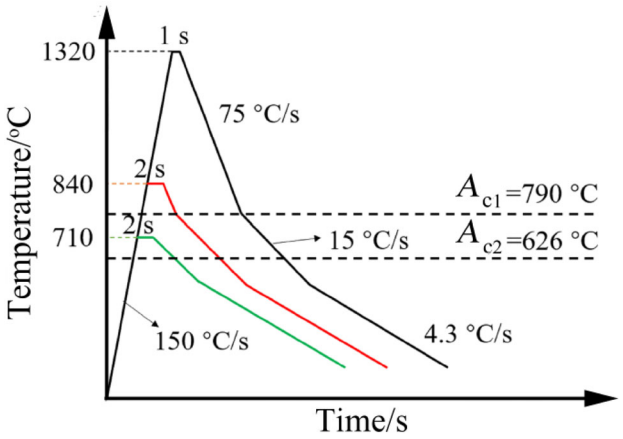

Fig. 1 Thermal simulation curves

Specimens for microscopic observations were cut from the heat-treated sample blank. Optical microscopy was performed to observe the microstructure using an Olympus BX51M microscope, and the etchant used was 4 vol.% nitric alcohol solution. The scanning electron microscope (SEM) equipped with electron backscattered diffraction (EBSD) was utilized to study the morphology and crystallography of the matrix. EBSD samples were electrolytically polished after grinding and polishing. The electrolyte was 5 vol.% perchloric alcohol solution, the voltage was 30 V, the current was 0.3 A, and the time was 40 s. Transmission electron microscopy (TEM) was carried out to study morphology and distribution of RA.

The grain size was determined using secant method. The appropriate position in the selected metallographic photograph is selected, and 3–5 line segments are drown. The length of the line segment is not less than one-third of the metallographic photograph to ensure that enough grains are measured. The grain size (D) is given by the following equation:

Table 1 Chemical composition of 5Mn steel (wt.%)

C	Si	Mn	S	P	Ni	Cr	Mo	Fe
0.06	0.20	5.10	≤ 0.0012	≤ 0.009	0.27	0.35	0.15	Balance

$$D = L/(MN) \quad (1)$$

where M is the magnification; N is the number of grains; and L is the length of the line segment.

The volume fraction of RA in thermally cycled specimens was determined using an X-ray diffractometer. The following equation was used to calculate the volume fraction V_γ:

$$V_\gamma = \frac{1}{1 + G\frac{I_{\alpha(hkl)}}{I_{\gamma(hkl)}}} \quad (2)$$

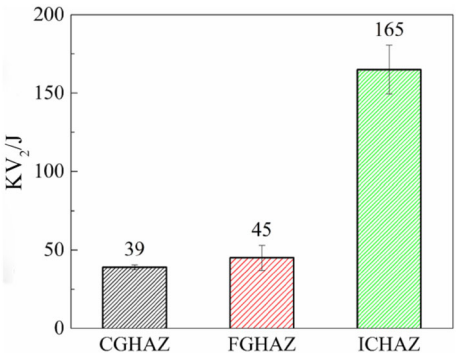

Fig. 2 Impact toughness in simulated HAZs at − 40 °C

where $I_{\alpha(hkl)}$ was intensity of martensitic crystal diffraction peaks; $I_{\gamma(hkl)}$ was intensity of austenite crystal diffraction peaks; and G was corresponding factor ratio of integrated intensities.

3 Results

3.1 Impact toughness in simulated HAZs

Figure 2 shows the impact toughness of simulated HAZs. The simulated CGHAZ had the lowest average absorbed energy of 39 J. For simulated FGHAZ, the mean absorbed energy was 45 J, which is slightly higher than that of the simulated CGHAZ. The highest average absorbed energy of 165 J was in the simulated ICHAZ. The mechanical property is determined by microstructure. Thus, the microstructural changes in the simulated HAZs were investigated.

3.2 Microstructure of simulated HAZs

The microstructures of simulated CGHAZ, FGHAZ and ICHAZ are martensite, as shown in Fig. 3. It can be seen that the prior austenite grain is larger in CGHAZ than in

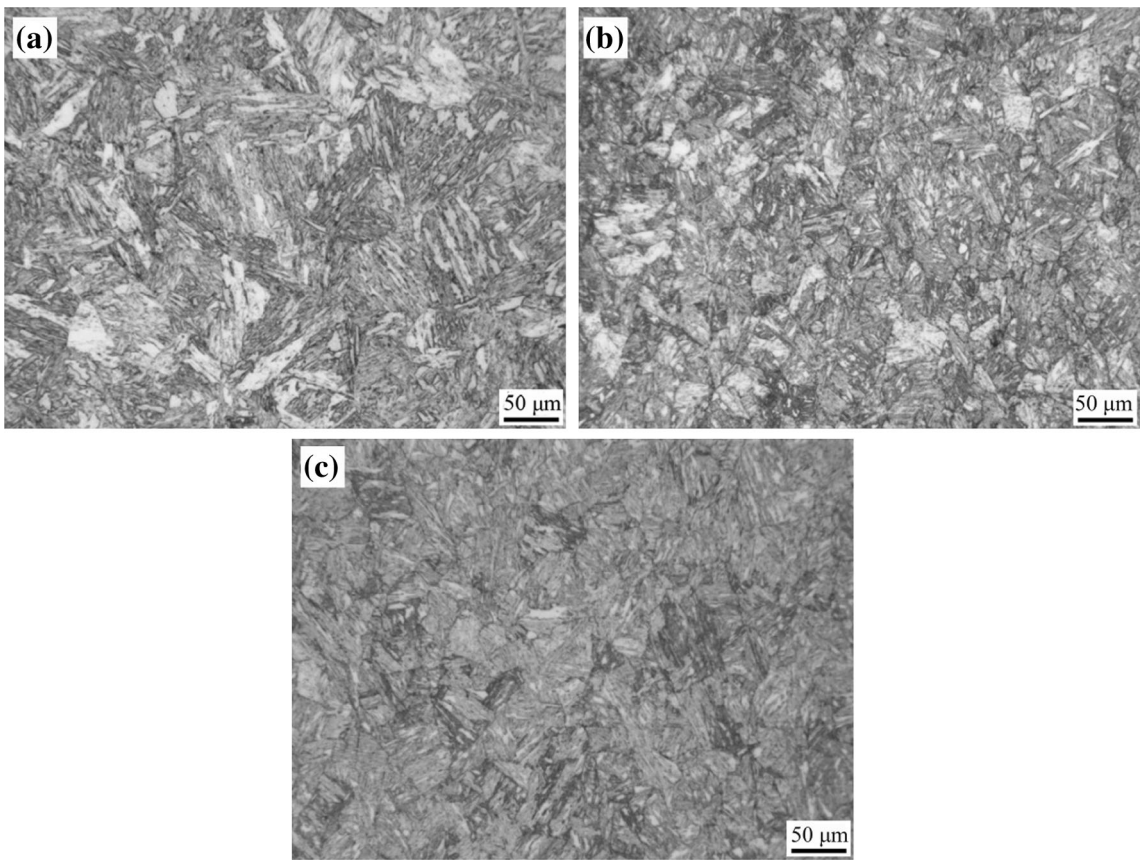

Fig. 3 Optical micrographs of simulated CGHAZ (**a**), FGHAZ (**b**) and ICHAZ (**c**)

FGHAZ and ICHAZ. However, martensite is classical lath-type structure, and its effective grain size is needed to be detected by EBSD.

3.3 Effective grain size in simulated HAZs

For lath-type martensite, the effective grain size is characterized by the block size [23] with grain boundaries larger than 15°. Figure 4a shows that there were several packets in simulated CGHAZ, and the packets involved blocks. The block width was measured to be ~ 0.8–1.6 μm in packet 1 and ~ 1.6–2.4 μm in packet 2, respectively. Figure 4b revealed that the grain size was fine in simulated FGHAZ, and there was no packet with large-angle boundary in grain. In simulated ICHAZ, the maximum block width was ~ 3.2 μm and minimum was ~ 0.4 μm. Figure 4g shows that the frequency of the large-angle grain boundary larger than 15° of simulated CGHAZ was lower than those of simulated FGHAZ and ICHAZ. Moreover, the frequency of large-angle grain boundary larger than 15° of simulated FGHAZ was greater than that of simulated ICHAZ, indicating that the effective grain size of simulated FGHAZ was smallest.

3.4 Volume fraction of RA in simulated HAZs

On subjecting to welding thermal cycling, RA is expected to alter in the simulated HAZs. X-ray diffraction (XRD) results of measurement of RA in simulated HAZs are given in Fig. 5. Only 1.2 vol.% austenite was detected in the simulated CGHAZ. Austenite peak in simulated FGHAZ and ICHAZ was clear, and the peak intensity was similar. The austenite content in simulated FGHAZ and ICHAZ was measured to be 11.6 and 11.5 vol.%, respectively.

3.5 Distribution and morphology of RA in simulated HAZs

Figure 6 shows that thin film-like structure was present along the martensite laths. In simulated FGHAZ, the thickness was ~ 100–130 nm. By selected area diffraction pattern (SADP, shown in Fig. 6d), the film-like structure was identified to be face centered cubic.

Similarly, thin film-like structure was observed along the martensite laths (Fig. 7). In simulated ICHAZ, the thickness was ~ 100–125 nm thinner than that in simulated FGHAZ. The diffraction pattern confirmed the film-like structure to be face centered cubic. TEM results demonstrated that the morphology of RA was similar in simulated FGHAZ and ICHAZ.

3.6 Distribution of Mn and Ni in RA

The distribution of Mn and Ni concentrations in RA (Fig. 8) in simulated FGHAZ and ICHAZ was studied to estimate the stability of RA. The concentration of Mn increased from the interface between martensite and retained austenite to the core of retained austenite. The maximum concentration in the austenite core was 8.89 and 8.75 wt.% in simulated FGHAZ and ICHAZ, respectively. Small enrichment of Ni in austenite was seen in simulated FGHAZ, while no enrichment of Ni was present in simulated ICHAZ. Mn and Ni concentrations in austenite implied similar stability of RA in simulated FGHAZ and ICHAZ [18, 19]. Until now, no distinct changes in volume fraction, morphology and stability of RA were observed in simulated FGHAZ and ICHAZ.

3.7 Martensite in simulated HAZs

Figure 9a shows that the microstructure of simulated FGHAZ mainly consisted of fresh martensite. The fresh martensite was characterized by long and straight laths and clear lath boundaries. The microstructure in simulated ICHAZ (Fig. 9b) consisted of tempered martensite and fresh martensite. At the peak temperature of 710 °C, martensite partially reversed into austenite and untransformed martensite was tempered. During subsequent cooling, significant amount of reversed austenite transformed into fresh martensite. Thus, fresh martensite and tempered martensite were obtained. Therefore, simulated FGHAZ mainly consisted of fresh martensite, while simulated ICHAZ consisted of both fresh and tempered martensite.

4 Discussion

4.1 Effect of effective grain size on impact toughness

The simulated CGHAZ had the lowest impact toughness of ~ 39 J, compared to ~ 45 J in the simulated FGHAZ and ~ 165 J in simulated ICHAZ.

On subjecting to welding thermal cycle at the peak temperature of 1320 °C, transformation to austenite occurs and austenite grains grow. Thus, coarse grains and the lowest frequency of large-angle grain boundaries were present in simulated CGHAZ. In simulated FGHAZ, although transformation to austenite was complete, austenite grains cannot grow at the peak temperature of 840 °C, which is slightly above A_{c3}. Thus, fine-grains were observed in the simulated FGHAZ. In simulated ICHAZ,

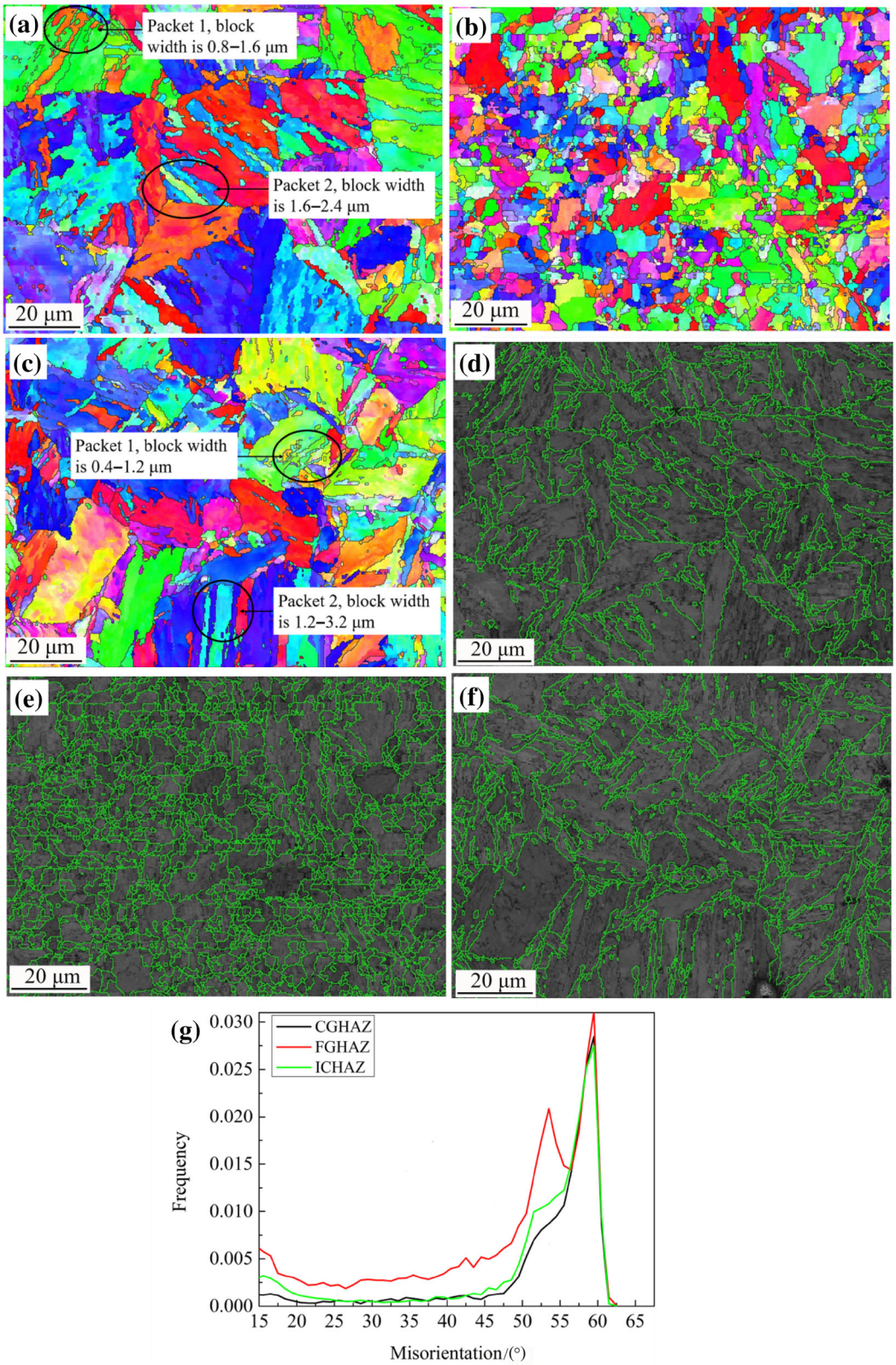

Fig. 4 Crystallographic analysis of simulated CGHAZ (**a**), FGHAZ (**b**) and ICHAZ (**c**), EBSD superimposed figures of band contrast and grain boundaries (misorientation > 15° in green line) of simulated CGHAZ (**d**), FGHAZ (**e**) and ICHAZ (**f**), and curves of misorientation angle-relative frequency of simulated HAZs (**g**)

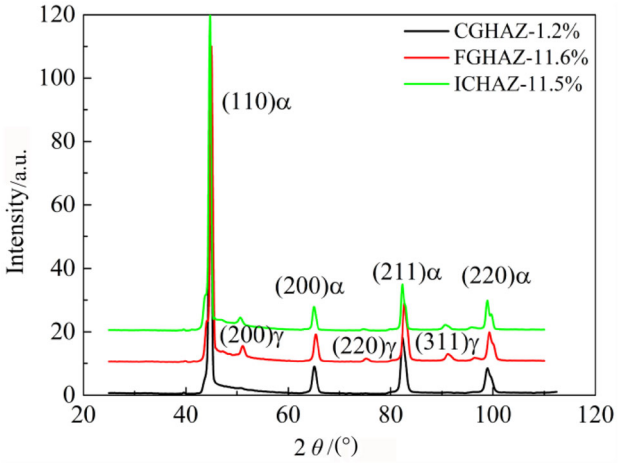

Fig. 5 XRD patterns of 5Mn steel in simulated HAZs

partial reverse transformation to austenite took place during welding thermal cycle at the peak temperature between A_{c1} and A_{c3}. Fine-grained structure was also observed in simulated ICHAZ.

Effective grain size is an important factor affecting the impact toughness. According to previous studies [24], the cleavage fracture strength conforms to the Hall–Petch relationship and can be expressed as:

$$\sigma_f = K_f d_{eff}^{-1/2} \tag{3}$$

where d_{eff} is the effective grain size that affects the impact toughness; σ_f is the yield strength; and K_f is the constant, which is related to the nature of the material and the grain size. The smaller the effective grain size, the superior the impact toughness is. The effective grain size of simulated

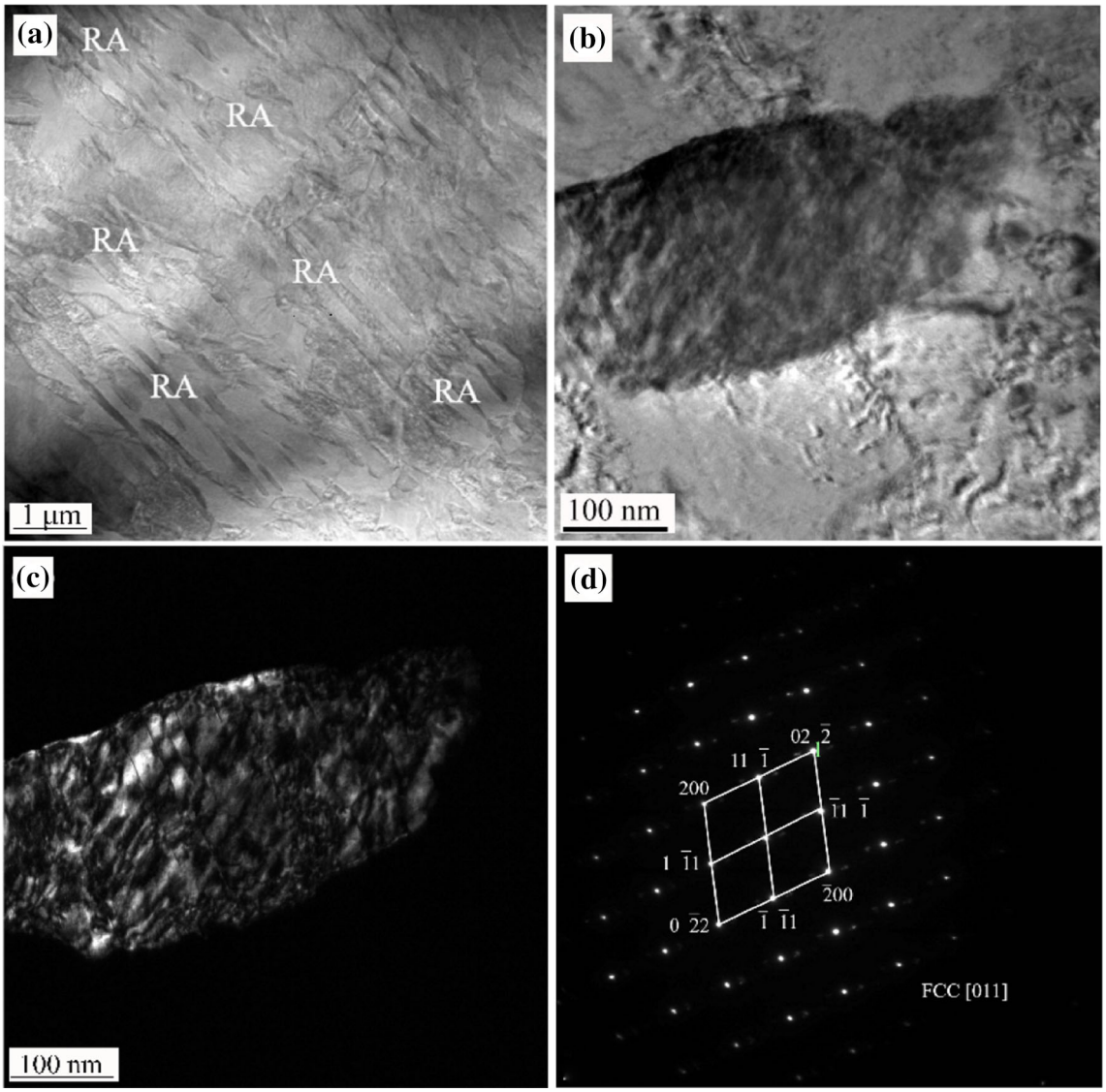

Fig. 6 TEM images of RA in simulated FGHAZ. **a** Distribution and morphology of RA; **b** bright-field TEM image of RA; **c** dark-field TEM image of RA; **d** SADP of RA structure

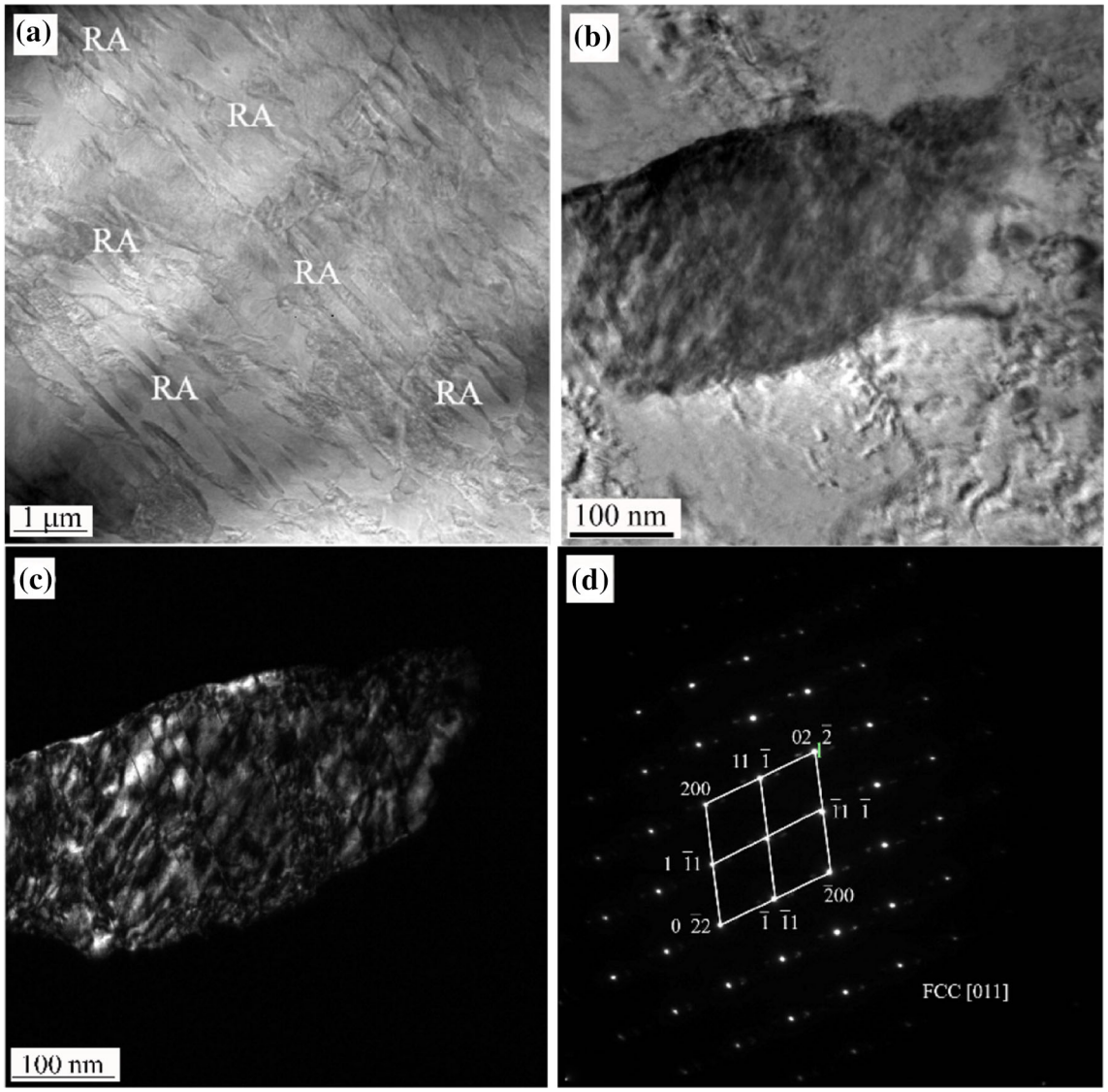

Fig. 7 TEM images of RA in simulated ICHAZ. **a** Distribution and morphology of RA; **b** bright-field TEM image of RA; **c** dark-field TEM image of RA; **d** SADP of RA structure

CGHAZ was largest compared to those of simulated FGHAZ and ICHAZ, resulting in low impact toughness.

Although the effective grain size of simulated FGHAZ was smaller than that of simulated ICHAZ, the impact toughness of simulated ICHAZ was higher than that of the simulated FGHAZ. The effect of volume fraction and stability of RA needs consideration to explain toughness.

4.2 Effect of volume fraction and stability of RA on impact toughness

Volume fraction of RA effectively affects the impact toughness [25, 26]. During the impact process, the austenite transforms into martensite (transformation-induced plasticity effect), alleviating the strain concentration in the martensite lath [21, 27]. On the other hand, the newly formed martensite with high hardness provides more second phase interface. It is conducive to the formation of dimples, which in turn helps to enhance the crack propagation work during the impact process [28]. Thus, the stress is relieved and the crack is blocked resulting in improvement of cryogenic impact toughness. XRD result showed that simulated CGHAZ contained only 1.2 vol.% RA, while simulated FGHAZ and ICHAZ had the high RA of 11.6 and 11.5 vol.%, respectively. In respective of volume fraction, simulated CGHAZ had the lowest impact toughness.

The stability of RA is another important role in affecting the impact toughness. In the impact process, the more stable RA, less likely it will transform to martensite. The

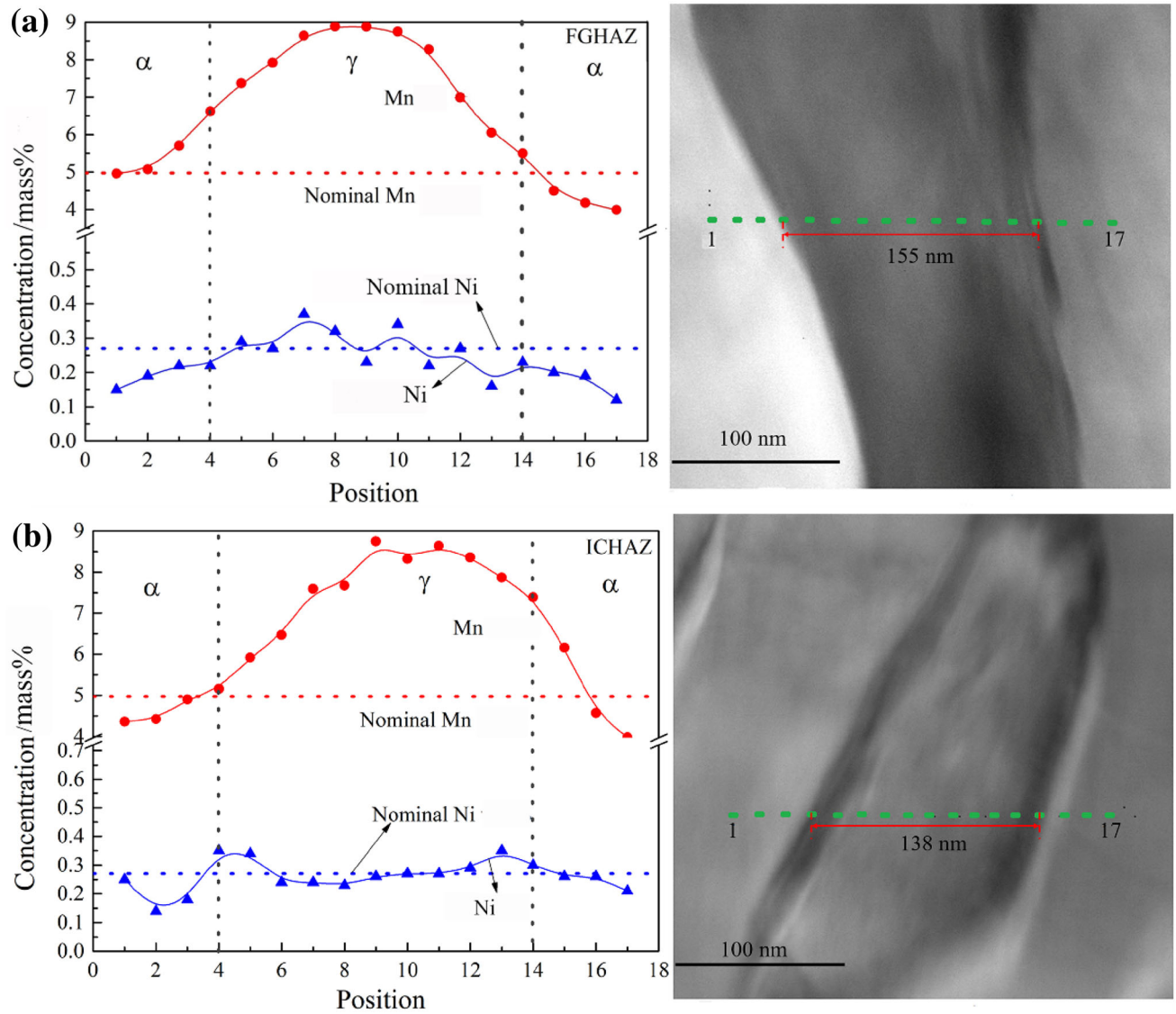

Fig. 8 EDS line-scan along green line in RA of simulated FGHAZ and ICHAZ

stable RA can greatly enhance the plastic deformation ability prior to initiation of crack, such that more energy is required to initiate cracks, and obtain excellent impact toughness [21]. It has been shown that element enrichment and size affect the stability of RA [18, 29]. In the present study, maximum Mn concentration in the core of RA was 8.89 wt.% in simulated FGHAZ and 8.75 wt.% in simulated ICHAZ. Ni was not enriched in the core of RA. The size of RA in simulated ICHAZ was smaller compared to that in simulated FGHAZ. Thus, it can be expected that the stability of RA in simulated ICHAZ was slightly greater than that in the simulated FGHAZ. However, the impact toughness of simulated ICHAZ was apparently superior than that of simulated FGHAZ. Thus, the effect of phase composition on impact toughness merits consideration.

4.3 Effect of phase constitution on impact toughness

The content of reversed austenite was studied by dilatometry. The tested specimen was cut from the quenched steel. From the dilatation–temperature curve, the volume fraction of the austenite at different temperatures was calculated using Eq. (4):

$$V = (\Delta L - \Delta L_\gamma)/(\Delta L_\alpha - \Delta L_\gamma) \quad (4)$$

where V is the austenite volume fraction; ΔL_α and ΔL_γ represent the extrapolated dilatations in the low-temperature and high-temperature range, respectively; and ΔL represents the extrapolated dilatations at temperature T. The austenite volume fraction as a function of temperature determined by dilatometry is presented in Fig. 10b.

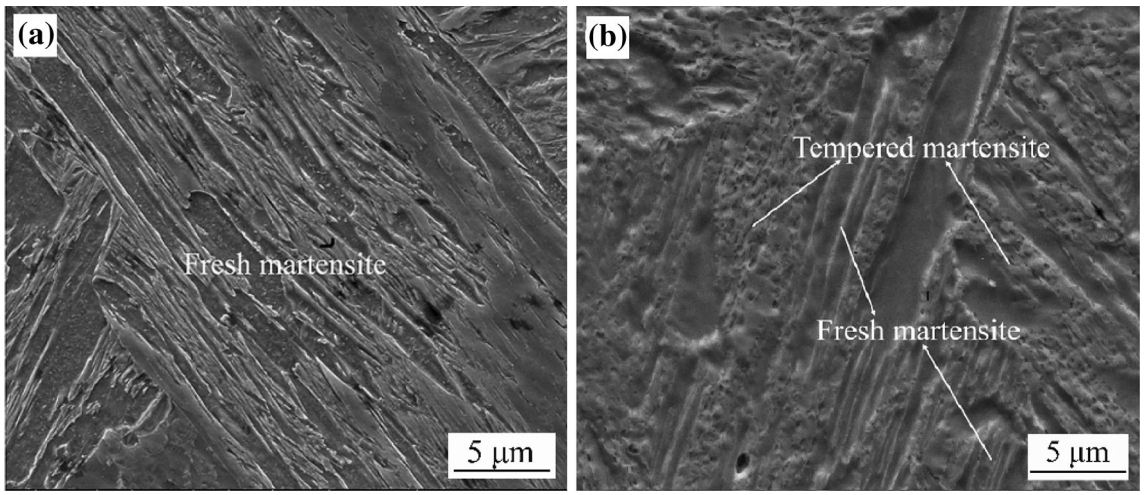

Fig. 9 SEM micrographs of simulated FGHAZ (**a**) and ICHAZ (**b**)

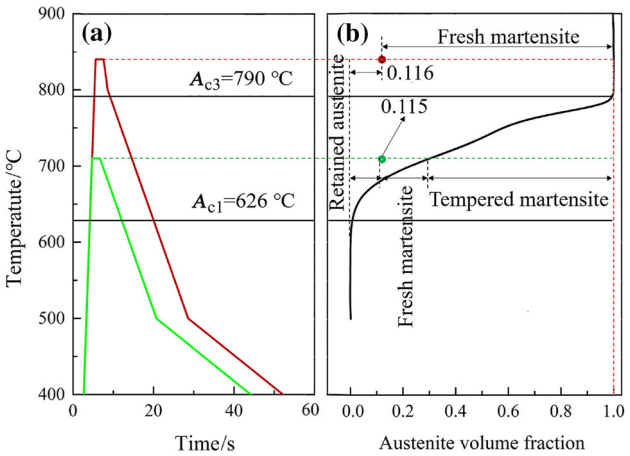

Fig. 10 Schematic of simulated welding thermal cycle (**a**) and variation of austenite volume fraction with temperature (**b**)

Schematic of welding thermal cycle corresponding to the volume fraction of austenite is plotted in Fig. 10. In the case of simulated FGHAZ, transformation to austenite was completed at the peak temperature of 840 °C. On subsequent fast cooling, 11.6 vol.% reversed austenite was retained, and 88.4 vol.% reversed austenite transformed to fresh martensite. For simulated ICHAZ, reverse transformation partially occurred at the peak temperature of 710 °C. Non-reversed martensite was tempered. Subsequently, besides 11.5 vol.% of RA, only small part of reversed austenite was transformed to fresh martensite on subsequent cooling. Fresh martensite has a high dislocation density and high distortion energy, in a manner similar to quenched martensite, which promotes the formation and propagation of crack during impact, thereby greatly reducing the toughness [29, 30]. Tempered martensite can hinder the expansion of crack [31]. Therefore, toughness is increased, such that the impact toughness of simulated ICHAZ was significantly better than that of the simulated FGHAZ.

5 Conclusions

1. Simulated CGHAZ had a lower absorbed energy of ~ 39 J at − 40 °C and was a consequence of coarse-grained structure and least volume fraction of retained austenite of 1.2 vol.%.
2. Simulated FGHAZ had the smallest effective grain size and simulated ICHAZ and FGHAZ had similar volume fraction of retained austenite and similar stability of RA. However, simulated ICHAZ had higher absorbed energy of ~ 165 J compared to ~ 45 J of simulated FGHAZ.
3. The good impact toughness in simulated ICHAZ is attributed to higher content of tempered martensite compared to simulated FGHAZ.

Acknowledgements Authors gratefully acknowledge the support from National Natural Science Foundation of China (No. 2015AA03A501).

References

[1] A. Ito, A. Shibata, N. Tsuji, Mater. Sci. Forum 879 (2016) 90–94.
[2] W. Wu, Y.W. Wang, P. Makrygiannis, F. Zhu, G.A. Thomas, L.G. Hector Jr., X.H. Hu, X. Sun, Y. Ren, Mater. Sci. Eng. A 711 (2018) 611–623.
[3] H.N. Han, C.S. Oh, G. Kim, O. Kwon, Mater. Sci. Eng. A 499 (2009) 462–468.
[4] O. Dmitrieva, D. Ponge, G. Inden, J. Millán, P. Choi, J. Sietsma, D. Raabe, Acta Mater. 59 (2011) 364–374.
[5] D.A. Porter, K.E. Easterling, M. Sherif, Phase transformation in metals and alloys, 3rd ed., CRC Press, Boca Raton, USA, 2009.

[6] H. Liu, L.X. Du, J. Hu, H.Y. Wu, X.H. Gao, R.D.K. Misra, J. Alloy. Compd. 695 (2017) 2072–2082.
[7] J. Chiang, B. Lawrence, J.D. Boyd, A.K. Pilkey, Mater. Sci. Eng. A 528 (2011) 4516–4521.
[8] J. Hu, L.X. Du, H. Liu, G.S. Sun, H. Xie, H.L. Yi, R.D.K. Misra, Mater. Sci. Eng. A 647 (2015) 144–151.
[9] J. Hu, L.X. Du, G.S. Sun, H. Xie, R.D.K. Misra, Scripta Mater. 104 (2015) 87–90.
[10] H. Shirazi, G. Miyamoto, S.H. Nedjad, H.G. Nanesa, M.N. Ahmadabadi, T. Furuhara, J. Alloy. Compd. 577 (2013) S572–S577.
[11] N. Nakada, K. Mizutani, T. Tsuchiyama, S. Takaki, Acta Mater. 65 (2014) 251–258.
[12] L. Jiang, X.J. Sun, Z.D. Li, Q.L. Yong, Iron and Steel 49 (2014) No. 12, 59–64.
[13] Y.L. Zhang, L. Wang, K.O. Findley, J.G. Speer, Metall. Mater. Trans. A 48 (2017) 2140–2149.
[14] J. Zhang, D.F. Chen, C.Q. Zhang, W.S. Hwang, M.R. Han, J. Mater. Res. 30 (2015) 2081–2089.
[15] P. Záhumenský, I. Kohútek, J. Semeňák, Mater. Sci. Eng. 283 (2017) 012024.
[16] X.J. Di, M. Li, Z.W. Yang, B.S. Wang, X.J. Guo, Mater. Des. 96 (2016) 232–240.
[17] A. Emamian, M. Alimardani, A. Khajepour, J. Manuf. Process 16 (2014) 511–517.
[18] S. Lee, S.J. Lee, B.C.D. Cooman, Scripta Mater. 65 (2011) 225–228.
[19] D. Jain, D. Isheim, X.J. Zhang, G. Ghosh, D.N. Seidman, Metall. Mater. Trans. A 48 (2017) 3642–3654.
[20] Z.C. Li, H. Ding, R.D.K. Misra, Z.H. Cai, Mater. Sci. Eng. A 682 (2017) 211–219.
[21] Z.J. Xie, S.F. Yuan, W.H. Zhou, J.R. Yang, H. Guo, C.J. Shang, Mater. Des. 59 (2014) 193–198.
[22] J. Yoo, K. Han, Y. Park, C. Lee, Mater. Chem. Phys. 146 (2014) 175–182.
[23] S. Morito, H. Yoshida, T. Maki, X. Huang, Mater. Sci. Eng. A 438-440 (2006) 237–240.
[24] C. Nagasaki, K. Matsui, K. Shibata, AIP Conference Proceedings 614 (2002) 139–145.
[25] J.A. da Cruz, J.J. Vilela, B.M. Gonzalez, D.B. Santos, Adv. Mater. Res. 922 (2014) 298–303.
[26] B.A. Tabatabae, F. Ashrafizadeh, A.M. Hassanl, ISIJ Int. 51 (2011) 471–475.
[27] B. Fultz, J.W. Morris, Metall. Trans. A 16 (1985) 173–177.
[28] J. Kang, C. Wang, G.D. Wang, Mater. Sci. Eng. A 553 (2012) 96–104.
[29] Q. Zhou, L.H. Qian, J. Tan, J. Meng, F. Zhang, Mater. Sci. Eng. A 578 (2013) 370–376.
[30] C. Sun, S.L. Liu, R.D.K. Misra, Q. Li, D.H. Li, Mater. Sci. Eng. A 711 (2018) 484–491.
[31] J. Chen, M.Y. Lv, Z.Y. Liu, G.D. Wang, Mater. Sci. Eng. A 648 (2015) 51–56.